



HAL
open science

X-ray tomographic image post-processing and a new 2D LBM simulation for the determination of the porosity and the static airflow resistivity of an acoustic fibrous material

Pierre Lamary, Belisario N Huallpa, Flávio C Bannwart, Enio P de Deus,
Ahmed Benallal, José R.F. Arruda

► To cite this version:

Pierre Lamary, Belisario N Huallpa, Flávio C Bannwart, Enio P de Deus, Ahmed Benallal, et al.. X-ray tomographic image post-processing and a new 2D LBM simulation for the determination of the porosity and the static airflow resistivity of an acoustic fibrous material. *Applied Acoustics*, 2020, 169, pp.107452. 10.1016/j.apacoust.2020.107452 . hal-03103044

HAL Id: hal-03103044

<https://hal.science/hal-03103044>

Submitted on 7 Jan 2021

HAL is a multi-disciplinary open access archive for the deposit and dissemination of scientific research documents, whether they are published or not. The documents may come from teaching and research institutions in France or abroad, or from public or private research centers.

L'archive ouverte pluridisciplinaire **HAL**, est destinée au dépôt et à la diffusion de documents scientifiques de niveau recherche, publiés ou non, émanant des établissements d'enseignement et de recherche français ou étrangers, des laboratoires publics ou privés.

X-ray tomographic image post-processing and a new 2D LBM simulation for the determination of the porosity and the static airflow resistivity of an acoustic fibrous material

Pierre Lamary^a, Belisario N. Hualpa^b, Flávio C. Bannwart^{c,1}, Enio P. de Deus^d, Ahmed Benallal^e, José R. F. Arruda^f

^aUFC, Department of Mechanical Engineering, Fortaleza, CE, Brazil

^bUFLA, Engineering Department, Lavras, MG, Brazil

^cUNICAMP, Department of Energy, Campinas, SP, Brazil

^dUFC, Department of Materials Engineering and Metallurgy, Fortaleza, CE, Brazil

^eLTM, ENS Paris-Saclay/CNRS/Université Paris-Saclay, France

^fUNICAMP, Department of Computational Mechanics, Campinas, SP, Brazil

Abstract

A set of X-ray tomographic images of a highly porous material composed of air-saturated coconut fibers is considered and used to estimate intrinsic characteristics of the material. Two physical properties are of interest: porosity and static airflow resistivity. For the porosity, two-dimensional gray-scale tomography images are obtained and post-processed to produce approximative black and white ones, unambiguously attributing distinct regions to fibers and air locations. The porosity is then directly deduced counting the black and white pixels. Several image processing algorithms are compared and associated porosities range from 0.76 to 0.97, depending on the method employed, while it is estimated to be 0.86 from our analysis. For the airflow resistivity, the idea followed here is to use the pattern of the post-processed images as the lattice in a Lattice Boltzmann Method (LBM) fluid dynamics computation. To our knowledge, the LBM has not been used in this context before. A new 2D implementation of the method is therefore developed and studied. After tuning computational parameters, we have estimated the airflow resistivity using ten images of our sample to be $1382 \pm 12 Pa.s/m^2$. Both porosity and resistivity results are fully consistent with measurements obtained from a porosity-meter and a resistivity-meter, demonstrating the pertinence of X-ray tomography and the associated proposed methods.

Keywords: porous material characterization, JCA model, X-ray image thresholding, Darcy's law, Lattice Boltzmann Method, mesoscale simulation.

1. Introduction

Acoustic porous materials are generally defined as composed of solid and fluid phases. Waves propagating in the fluid are attenuated when passing through the open pores due to viscous and thermal dissipation mechanisms, besides the structural dissipation due to the solid frame elastic deformation. This acoustic energy attenuation can be modeled using Biot's theory [1].

10 A relevant aspect of Biot's theory is the homogenized equations. Allard [2] and other authors applied it to acoustic materials and proposed frequency domain dynamic equations coupling the fluid and structural phases. The reader can refer to [3] for a recent review of acoustical methods for porous media or to [4] for a multi-physic approach to porosity. In the limiting cases where the solid frame is considered rigid or when its stiffness is considered negligible (limp models), an equivalent fluid model can be alternatively used. For characterization purposes, these models are interesting since they include all acoustic dissipation mechanisms while still remaining simple. In this

¹Corresponding author at: Rua Mendeleev, 200, Campinas, SP, CEP: 13083-860, Brazil. Email address: fcbannwart@fem.unicamp.br

study, the equivalent fluid model applies without
25 restriction because we pay attention to two param-
eters, the porosity and the static airflow resistiv-
ity, that can be characterized considering the static
or quasi-static behavior of the material. The fre-
quency tends to zero and, consequently, there is no
30 vibration of the structural skeleton.

For the Biot-Allard's theory, the relevant aspect
concerns the coefficients involved in the homogen-
ized equations. They are expressed as frequency
domain functions. Several models are available, and
35 the Johnson-Champoux-Allard (JCA) micro-macro
model is considered here. The JCA model involves
five physical parameters: porosity, tortuosity, static
airflow resistivity, viscous and thermal characteris-
tic lengths. They are interrelated by two complex
40 valued equations (Eqs. 2 and 4), in which two pa-
rameters are known, especially the porosity and the
static airflow resistivity. The remaining three pa-
rameters may be obtained experimentally, for in-
stance using indirect methods, such as the ones in-
volving acoustic impedance tubes [5, 6, 7], or using
45 inverse acoustical methods [8, 9, 10, 11]. Other au-
thors [12] [13] [14] [15] investigate theoretical, nu-
merical and empirical models for the airflow resis-
tivity involving a restrained set of parameters, such
as the fiber diameter and its influence on sound ab-
50 sorption coefficients, the fiber bulk modulus, and
the porosity. In the works of [15], for instance, one
important conclusion was that the nanofiber diam-
eter of a nano-fibrous material selected for study,
varying from 80 to 397nm, was not a key factor in
55 the determination of sound absorption coefficients.
Nevertheless, such a conclusion does not discourage
the investigations on airflow resistivities, as the con-
clusions may result completely different for this pa-
60 rameter. Our fibrous material, for instance, varies
on its fiber diameter ranging from around 50 μ m to
300 μ m, i.e, from the order of 1000 times larger than
in the case of [15], which turns the problem much
different.

The main purpose of this work is to provide a new
65 direct method of low computational cost to obtain
the airflow resistivity of natural fibrous materials
(intrinsically difficult to characterize and of sustain-
ability interest) from X-ray images. The driving
70 idea is to use the pixels of the image as the lattice of
the Lattice Boltzmann Method. Besides, from the
same X-ray images, we determine the corresponding
porosity. Therefore, the work is essentially twofold.

The starting point is the utilization of a set of
75 X-ray Computer Tomography (CT) images of a fi-

brous acoustic material to estimate its porosity (di-
rect method). The fibers are natural and were ob-
tained from the outer skin of coconuts. They were
sprayed with latex and compressed to form a fi-
brous material [16]. To process the resulting pile
of gray scale CT images, we apply the method pro-
posed in [17], where an algorithm attributes only
black or white color to each image pixel and gener-
ates a data histogram. Next, the post-processed
85 image is utilized to carry out 2D simulations with
the airflow resistivity as indicator, also consisting
in a direct method.

From a general point of view, experimental test
rigs consist of two main parts: physical devices
equipped with sensors, and numerical procedures
to transform the sensor information into meaningful
indicators. In this study, the physical device is an
X-ray tomography equipment, and the numerical
procedures are subsequent image post-processing
and 2D LBM simulations to estimate, respectively,
95 the porosity and the static airflow resistivity of a
porous sample. The originality and the novelty of
the work come from the fact that, to our knowl-
edge, the numerical procedures suggested here have
not been presented in the literature in the con-
text of acoustic characterization. In particular, for
what concerns the LBM method, the closest related
works were found in the field of soil mechanics with
the determination of the permeability of low porous
rocks saturated with liquid. Another related field
105 where advanced mesoscale calculation are carried
out is the field of homogenization; and we may cite
the works of [18, 19].

This paper is organized as follows: We first de-
scribe the investigated porous material and the ex-
perimental procedures; then, we present the acous-
tic indicators relative to the estimated ones fol-
lowing the Biot-Allard theory of poroelasticity; we
then propose the numerical methods to estimate
115 the porosity based on statistical techniques and the
static airflow resistivity using the LBM method
applied to fluid dynamics; the results obtained
with these proposed methods are then compared
with experimental values obtained directly using a
porosity-meter and a resistivity-meter. Discussions
of the results are provided all along the paper and
in the conclusion.

2. Materials and experimental procedures

2.1. Materials

125 The specimen used in this work was cut from
a board made of coconut fiber recovered with
natural latex produced by a local manufacturer
(Coquim, São Paulo, Brazil). The sample size
(50x50x50mm³) was selected in order to preserve
130 the characteristics of the original arrangement of
the compacted fibers and to allow measurement in
acoustic devices. The sample is shown in Figure 1.



Figure 1: Porous sample under study.

2.2. X-ray tomography

135 The X-ray tomography equipment used in this
study is the model X50 (Fig. 2) from the North
Star Imaging Company, Inc.. It consists of a pro-
tected radiation cabin, 5-axis manipulator, dual
X-ray tube of 225kV with dual source (reflection
and transmission), and a detector DEXELA 2923,
140 CMOS image sensor technology with scintillator
and interface options, plane cesium 3072 x 3888
pixel matrix, 14-bit and 26 frames/second at full
resolution. A software suite manages the data ac-
quisition, image processing and 3D reconstruction.
145 In this work, the molybdenum tube was set at
50kV, 150μA and 23.1W. The 1400 2D slices per-
pendicular to axis y (across the thickness of the
sample) were acquired at the average velocity of 10
frames/second.

150 Fig. 3 shows a 3D image reconstruction of the
sample of Fig. 1 provided by the software suite of
the X-ray tomography equipment.

2.3. Porosity-meter and resistivity-meter

155 In order to get reference values, our sample was
also characterized using two traditional devices, the



Figure 2: X-ray tomography equipment.

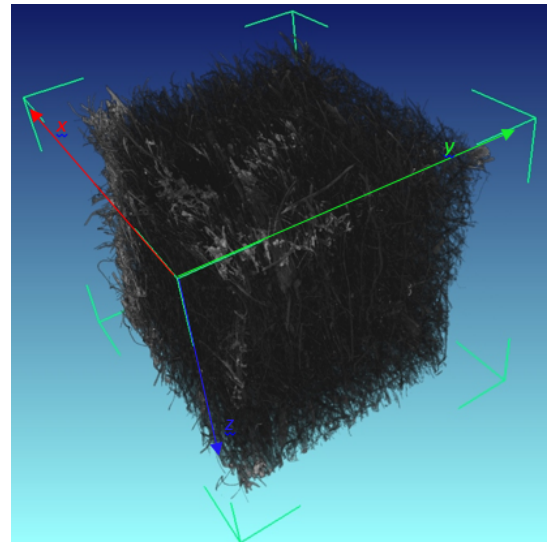


Figure 3: Tomographic 3D image reconstruction of the porous sample under study.

i) PHI – Porosity and Density Meter and the ii) HF SIGMA – High Airflow Resistance Meter developed by Mecanum Inc..

3. Porous material parameters

160 In this section, the JCA and fluid equivalent
models are introduced to recall and show how the
porosity and the resistivity parameters are embed-
ded in the formulation. It will be therefore needed
to solve the fluid equivalent model equation in order
165 to estimate the sensitivity of the material param-
eters toward the global acoustic indicators such as
the absorption and the transmission losses through
the porous sample. This will be done in the discus-
sion of paragraph 5.6.

170 The fluid equivalent model is generally obtained
 by a limiting process from the poro-elastic equa-
 tions, in particular, from the so-called (U, p) formu-
 lation. The reader will find many documents, as
 175 cited in this section, following this approach. To
 renew with the writing of this model and to give
 another physical insight, the fluid equivalent model
 is introduced here from the Helmholtz equation of
 acoustics.

3.1. Biot theory

180 Biot introduced homogenized equations for the
 modeling of the behavior of poroelastic and porous
 materials [1]. These equations can be written
 in the frequency domain and coupled with struc-
 tural dynamics and acoustics. Implemented in soft-
 185 ware based on semi-analytical methods such as the
 Transfer Matrix Method [20, 2, 21, 22, 23, 7], or
 based on numerical methods such as the Bound-
 ary Element Method [24] and the Finite Element
 Method [2, 25, 26], the Biot equations allow for
 190 the study of complex acoustic insulation systems.
 Without loss of generality, let us consider the equiv-
 alent fluid model, which gathers all the dissipative
 phenomena of interest here. The fluid consists of
 the fluid that can go through the open pores; the
 195 skeleton is motionless. Rigid motion of the skele-
 ton can be taken into account if needed for cou-
 pled problems, where the fluid-structure dynamic
 interaction is relevant; this model is referred to as
 equivalent fluid limp model.

200 From substitution of the behavior laws (stress-
 strain relations) in the dynamic motion equations,
 and using the acoustic pressure \tilde{p} as the main un-
 known, the fluid equivalent model reads as the fol-
 lowing Helmholtz equation:

$$\Delta \tilde{p} + \tilde{k}^2 \tilde{p} = 0, \quad (1)$$

205 where \tilde{k} is a lossy wavenumber, designated complex
 by the tilde notation ($\tilde{\cdot}$), employed throughout the
 text.

For an acoustic ideal fluid (without viscous losses
 or thermal relaxation) the differential equation (1)
 210 applies, and the classical acoustic equation is recov-
 ered, with \tilde{k} a real wavenumber defined as $\tilde{k} = k =$
 ω/c , where ω is the angular frequency and c the
 speed of sound. Associated boundary conditions
 are, $\tilde{p} = \bar{p}$, an imposed pressure at a given bound-
 215 ary, and $\partial \tilde{p} / \partial n = \rho_0 \omega^2 \bar{u}_n$, an imposed normal
 acoustic displacement at other boundaries, where

ρ_0 is the fluid density. If \bar{p} and \bar{u}_n are real, \tilde{p} be-
 comes therefore real as well. Internal dissipation
 can be introduced in this equation considering, for
 instance, a damping factor η applied to the acoustic
 bulk modulus K_0 as $\tilde{K} = K_0(1 + j\eta)$ (viscoelastic
 model), changing the definition of $c = \sqrt{K_0/c}$ to
 a complex speed of sound $\tilde{c} = \sqrt{\tilde{K}/\rho_0}$ and leading
 finally to a complex wavenumber $\tilde{k} = \omega/\tilde{c}$.

225 The Biot equivalent fluid model generalizes these
 definitions with $\tilde{c}(\omega) = \sqrt{\tilde{K}(\omega)/\tilde{\rho}(\omega)}$. When this
 model is considered to occupy the entire porous mat-
 erial, i.e. all the volume of the fluid in the pores
 and of the skeleton, the equivalent pertinent enti-
 ties are $\tilde{K}_{eq}(\omega) = \tilde{K}(\omega)/\phi$ and $\tilde{\rho}_{eq}(\omega) = \tilde{\rho}(\omega)/\phi$,
 where ϕ is the porosity. For instance, $\partial \tilde{p} / \partial n$ at the
 boundary has to be written $\partial \tilde{p} / \partial n = \tilde{\rho}_{eq}(\omega) \omega^2 \bar{u}_n$.

3.2. The JCA micro-macro model

235 The micro-macro models provide formulae to ex-
 press $\tilde{K}(\omega)$ and $\tilde{\rho}(\omega)$. Several micro-macro mod-
 els are presented in [2]. The simplest one is the
 Delany and Bazley model, which only requires the
 knowledge of the static airflow resistivity. Oth-
 ers are dedicated to specific pore geometries. One
 of special interest is the Johnson-Champoux-Allard
 (JCA) model, which gives good predictions for ran-
 dom pore distribution and is commonly adopted to-
 day.

240 In this model, $\tilde{\rho}(\omega)$ and $\tilde{K}(\omega)$ can be defined ac-
 cording to the formalism of [27] as:

$$\tilde{\rho}(\omega) = \alpha_\infty \rho_0 \left(1 + \frac{1}{j\tilde{\omega}} \sqrt{1 + j\tilde{G}(\omega)} \right), \quad (2)$$

with

$$\tilde{G}(\omega) = \sqrt{1 + j\frac{M}{2}\tilde{\omega}}, \quad (3)$$

where $\tilde{\omega} = \frac{\omega \alpha_\infty \rho_0}{\phi \sigma}$ is a dimensionless frequency, and
 $M = \frac{8\alpha_\infty \rho_0}{\phi \Lambda^2 \sigma}$ is a shape factor. And

$$\tilde{K}(\omega) = \frac{K_0}{\gamma - (\gamma - 1) \left(1 + \frac{8\eta}{j\omega \rho_0 N_{pr}^2 \Lambda'^2} \tilde{G}'(\omega) \right)^{-1}}, \quad (4)$$

with

$$\tilde{G}'(\omega) = \sqrt{1 + j\frac{\omega \rho_0 N_{pr}^2 \Lambda'^2}{16\eta}}. \quad (5)$$

250 The known entities are ρ_0 , K_0 , N_{pr} and γ - air
thermophysical properties. N_{pr} is the Prandtl num-
ber set to 0.71, and γ is the ratio of specific heats 300
taken to be 1.4. The JCA parameters are labeled
 ϕ , σ , α_∞ , Λ and Λ' , respectively: porosity, static
255 airflow resistivity, and viscous and thermal char-
acteristic lengths. From Eq. 2 one can note that $\tilde{\rho}(\omega)$
involves only the first four parameters of the model 305
and is linked to viscous effects, while, from Eq. 4,
 $\tilde{K}(\omega)$ involves the fifth and last parameter, linked
260 to thermal effects.

4. Estimating porosity from XRCT images 310

4.1. Porosity

Porosity is defined as the ratio of the volume oc-
cupied by the fluid phase (usually air) to the total 315
porous material volume, which also embraces the
solid frame phase [2]. Porosity must be measured or
computed for a representative volume of the acous-
tic material. A representative volume has a charac-
teristic length much smaller than the wavelength of 320
the waves in the audio frequency range and much
larger than the random microscopic features of the
material, so that average properties of the homog-
enized material can be obtained.

Traditional methods usually applied to experi-
mentally estimate porosity can be classified in two 275
types. Direct methods consist in the immersion of
a porous material sample in a incompressible fluid
(typically water) and computing the volume ratio
between the fluid phase and the entire sample [28].
280 Otherwise, if the mass density of the solid phase
is known and homogeneous, from the weight of the
sample, the volume of the solid frame can be com-
puted and subtracted from the total volume ob-
tained from the sample external geometry. More
285 precise methods are based upon gas expansion in
cavities with known volume and pressure measure-
ments, such as in the Boyle's Law Porosimeter [29].

4.2. X-ray CT 2D images

290 The directly obtained X-ray CT images reveal
2D transversal slices of a sample [30], sequentially
numbered. Each image is formed according to the
X-ray attenuation dependency on the local mate-
rial density through which the radiation is trans-
mitted. Using appropriate image processing trans- 340
formations, it is possible to create a 3D image from
295 slices of a material sample. For high energy X-rays
(above 100 kV) [17], those images are associated

to the so-called CT number and correlated to mass
density. Therefore, in principle it is possible to es-
timate the porosity of a sample of porous material
using CT images. If an acoustic material is com-
posed of solid and fluid (air) phases, the solid phase
is likely to have the higher density, which makes it
distinguishable by contrast. Evaluation of the pro-
portion between phases leads to determine the vol-
ume of air as a percentage of the total volume, i.e.
the porosity. Usual CT images are calibrated so
that water gives zero for its CT value, and air gives
-1000. The solid phase has values typically larger
310 than zero.

In acoustics, we are interested in the open porosity,
i.e., the domain of the material where an external
fluid can flow through. Therefore, closed pores,
where a fluid has been imprisoned when making the
material, have to be excluded. 2D images may arti-
ficially produce closed pores. However, from the
nature of our material, made of fibers, those pores
are likely to be open when the 3D situation is con-
sidered. Thus, we can count all the fluid part in the
2D images as open pores (white).

4.3. Thresholding

The major problem for estimating porosity from
CT images is the segmentation process (threshold-
ing) in order to separate air from solid. Visual
thresholding is prone to subjective errors and lacks
repeatability. A recent work by [17] proposes a
method based upon CT images to estimate porosity.
Given a set of images constituting the scan of a
representative volume of the porous material, to
each pixel (or voxel, in the 3D case) of the image,
a CT number ranging from 0 to r_{max} is attributed.
They are typically gray scale image integer values.
The range of CT values is divided into bins, and
a histogram is computed, so that to each range of
values r_i , $(i-1)\Delta r < r_i < i\Delta r$, has a count of
335 n_i in a total number of pixels (or voxels) of n , with
 $H(r_i) = n_i/n$ and $\sum_{r_i=0}^{r_{max}} H(r_i) = 1$. In this case
the porosity can be estimated with:

$$\Phi(r_{max}) = \frac{\sum_{r_i=0}^{r_{max}} (r_{max} - r_i) H(r_i)}{\sum_{r_i=0}^{r_{max}} r_{max} H(r_i)}. \quad (6)$$

340 This value is computed for different values of
 r_{max} , and the minimum of the obtained curve cor-
responds to the desired porosity. Depending on how
the image is processed, the value of $1 - \Phi$ can be
obtained, as it is the case in the example treated in

345 this work. The results obtained with this method (labeled later on as "Our analysis") are compared with the classical methods based on the thresholding approach, such as IsoData [31], Huang [32], Li [33], Mean [34], Moments [35], Otsu [36], and Shanbhag [37], as shown in Table 1. These thresholding methods are available in the public open domain ImageJ program (www.imagej.net) used in this work.

4.4. Porosity estimation results

355 A coconut fiber sample measuring approximately $50 \times 50 \times 50 \text{ mm}^3$ was placed in a X-ray CT, and 1158 slices were measured. We have observed that the slices with low data acquisition noise, slightly apart from the cut surfaces, were numbered between 150 and 939, which means 790 slices. After selecting the slices and applying a crop process, a 3D cube with dimensions of $40 \times 40 \times 40 \text{ mm}^3$ and with voxel size of $46.1 \times 46.1 \times 46.1 \mu\text{m}^3$ was selected.

360 Figure 4 shows the X-ray CT cropped 3D image of the coconut fiber material. The initial specimen size of $50 \times 50 \times 45 \text{ mm}^3$ (Fig. 3) was reduced to a final size of $40 \times 40 \times 40 \text{ mm}^3$.

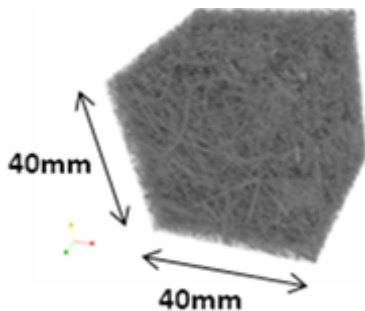


Figure 4: XRCT 3D cropped image.

370 The dimension of a slice of this 3D image is therefore $40 \times 40 \text{ mm}^2$ with a pixel size of $46.1 \times 46.1 \mu\text{m}^2$. The thickness is $46.1 \mu\text{m}$. In the following, we will indifferently call a slice of unit pixel thickness, a slice or a 2D image. Figure 5 shows a slice image. The clear spots correspond to the denser material (fiber), while the dark gray are the pores (fluid). Then, the 2D images were submitted to the thresholding process (transformation of the gray scale image to binary scale) using different methods that software imageJ offers. The methods used were IsoData, IJ-IsoData, Li, MaxEntropy, Mean, Moments, Huang, Otsu, and Shanbhag. After selecting

380 the threshold method (binarization), which permits the conversion to black and white pixels, the porosity can be computed. Black pixels are associated with the skeleton and white pixels to the fluid. The porosity is given by the ratio of the number of white pixels and total of number of white and black pixels. Figure 6 shows the result obtained when using the Otsu's thresholding method.

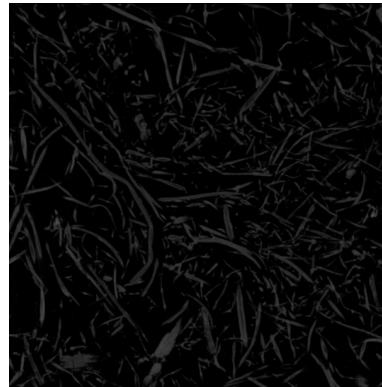


Figure 5: Original image.

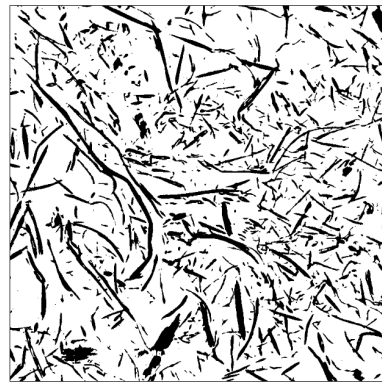


Figure 6: Processed image.

390 Table 1 shows the results of the porosity values for the different threshold methods. It can be observed that different threshold methods yield different values for porosity. The values of the porosity present a range of variation between 0.76 and 0.96, which means a dispersion of 0.2. Huang, Li, and Mean methods present lower values, in opposition to Moments and Shanbhag methods. The value of 0.87, labeled as RefTest (Reference Test), is the one obtained when using a porosity-meter.

400 To apply the histogram-based grey scale image method proposed by [17], the CT image was read within MATLAB© and a histogram with 100 bins was built, as shown in Fig. 7. The resulting porosity

Table 1: Results of porosity using different thresholding methods.

Method	Our analysis	Huang	Isodata
Porosity	0.86	0.78	0.83
Method	Max Entropy	Mean	Moments
Porosity	0.82	0.78	0.93
Method	Li	Otsu	Shanbhag
Porosity	0.78	0.85	0.97
Method	RefTest		
Porosity	0.87		

values obtained for the first slice (number 150) are shown in Fig. 8. Being restricted to one slice, this plot is not conclusive, as many local minima are present. Proceeding with the computation of this curve for all 790 slices of the sample and averaging, as presented on the plot of Fig. 9, the porosity can be estimated to be 0.86. When compared to the others methods (Table 1), our analysis provides the closest value to the measured one of 0.87 (RefTest).

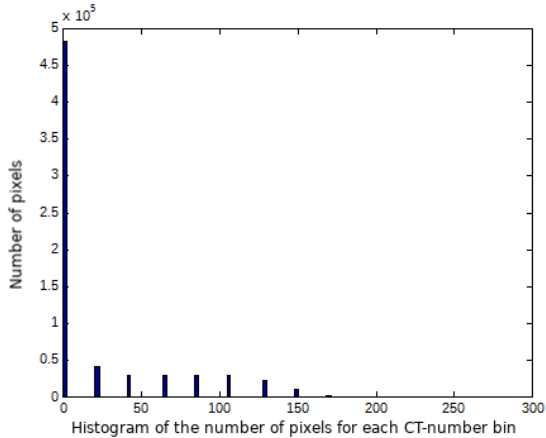


Figure 7: Tomographic 3D image reconstruction of a porous sample under study.

4.5. Discussion

The proposed method draws benefit from the detailed information coming from the tomographic images, i.e., it uses all pixels constituting the volume of the sample. Doing this, and as shown by the results obtained, the method allows the accurate prediction of the porosity of the sample.

Furthermore, the different thresholding methods used to estimate porosity can produce the black and

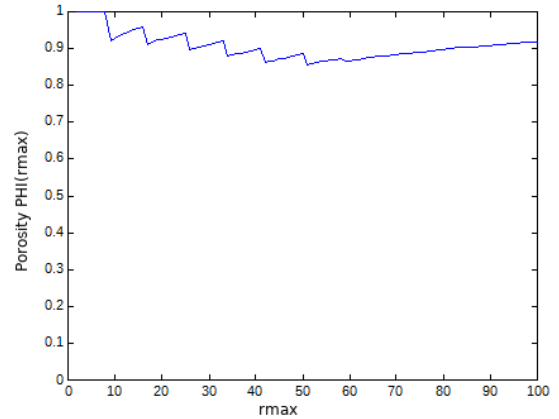


Figure 8: Estimating porosity from one slice with the method proposed in [17].

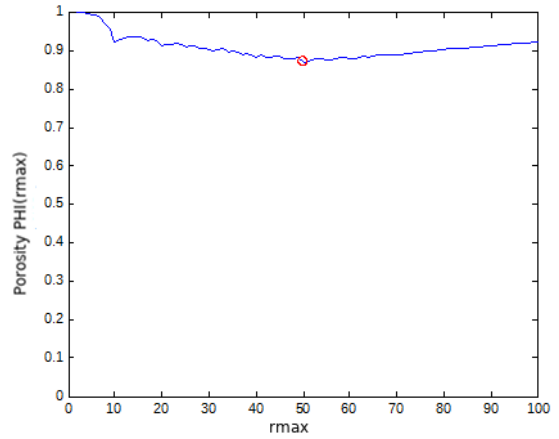


Figure 9: Estimating porosity from 790 slices with the method proposed in [17].

white images needed in the following section concerning the use of the LBM method to estimate the resistivity of the sample. Therefore, it is suggested to use the best suitable alternative thresholding method, which yields the closest value to the proposed method, to produce black and white images of the sample. From the analysis results synthesized in Table 1, the best suitable candidate is the Otsu's method, which will be used in the following section.

5. Estimating the airflow resistivity using 2D LBM simulation

Semi-analytical phenomenological micro-macro models, such as the JCA model, are developed considering the Poiseuille type flow, which is the type of flow that LBM solves in its basic assumptions (laminar flow). However, the objective of this work is not to completely substitute the micro-macro model by LBM calculations - since it would require the consideration of the coupling factor and parameters involved in the frame of Biot theory as frequency functions, an entanglement beyond our interest for now. Instead, the objective here is determination of just one of the five parameters needed to fulfill the JCA model, which is the static airflow resistivity. This parameter is obtained for very slow airflow. In this regime, the velocity of the airflow is proportional to pressure drop along the sample leading to a constant value for the resistivity, i.e., independent of the velocity of the flow. Classical experimental methods to determine the airflow resistivity use a resistivity-meter [22].

5.1. Darcy permeability and airflow resistivity

When fluid goes slowly through pores, resistive phenomena induced by viscous friction are predominant and those forces balance with the fluid velocity. The pertinent parameter to describe this phenomena is the permeability of the medium, which is expressed by the Darcy's law. Written in an up-to-date form, the permeability \mathbf{k} is a second order tensor that we may write in Cartesian coordinates as

$$k_{ij} = -\frac{\eta}{p_{,j}} \langle v_i \rangle, \quad (7)$$

where v_i is the outflow speed field in the i direction, $\langle \rangle$ is the volume average, $\langle v_i \rangle = \phi \frac{\int_A v_i da}{\int_A da}$, with ϕ being the porosity and A being the area in 2D (or the volume in 3D) of the fluid part, and $p_{,j}$ is the gradient pressure in the j direction. This gradient applies as a field all over the wet fluid domain.

From this, the static airflow resistivity σ , which is also a second order tensor, can be related to \mathbf{k} as

$$\sigma_{ij} = \eta(k_{ij})^{-1}. \quad (8)$$

An acoustic material is generally manufactured in layer form, and the fabrication process may turn the layer orthotropic. If its principal directions are priorly known, tests or computation shall be carried

out in those directions to directly express Eqs. 8 and 9, for instance. The permeability and resistivity tensors also possess the propriety of symmetry. The reader can refer to [38], where experimental and numerical procedures are presented to characterize anisotropic materials.

Neglecting the non-diagonal terms of \mathbf{k} , Eq. 8 can be solved as

$$\sigma_{ii} = \frac{\eta}{k_{ii}}, \quad (9)$$

with $i \in \{1, 2\}$ for our 2D simulations. The mean value of the tensor defined as $\sigma = (\sigma_{11} + \sigma_{22})/2$ is considered as our final indicator. To recover the 3D situation, several slices of a sample are considered, each slice being a 2D image treated by a 2D calculation. Statistic mean values are given to approximate the global resistivity of the 3D sample.

5.2. The numerical model

The numerical model is inspired by the resistivity-meter configuration and is sometimes called numerical tube. It consists, see Fig. 10, in the 2D image sample to be computed, two side impervious rigid walls, and two fluid buffers: inlet and outlet. The dimensions are given in number of pixels. For the analysis presented further on, the 2D images are of 821×821 pixels (each pixel sized $46.1 \times 46.1 \mu m^2$), and the remaining parts are two pixels thick. A pressure gradient, oriented in the longitudinal direction of the tube (direction 1, in Fig. 10) is imposed along the entire domain of the model, and the LBM algorithm computes iteratively the corresponding velocity field, from which, the resistivity (in this direction) is deduced. To get the resistivity in the direction 2, the porous sample is simply rotated at an angle of 90° .

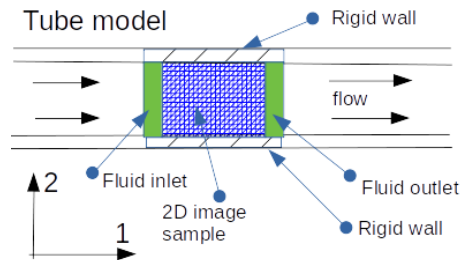


Figure 10: 2D numerical model.

From a technical point of view, the LBM algorithm implemented in this work refers to the LBM-BGK method with D2Q9 cells and a direct

bounce-back scheme. Bounce-back occurs when the fluid in question meets a rigid obstacle such as the side walls and the fibers of the material. These choices correspond to one of a most simple implementation of LBM. The reader can refer to Appendix A to access the algorithm we used in this study. The full script of the program is also available and can be found in the following repository (<http://www.labvib.ufc.br/CavLBM.html>).

5.3. Physical units and LBM units

5.3.1. Basic conversions

Many studies using LBM concern the enhancement of the method, and their results are presented in Lattice units. To solve physical problems, physical units shall be converted to Lattice units and, next, shall express the LBM results in physical units. The conference paper [39] focuses on this aspect and presents a clear methodology. Conversion factors are established for the fundamental entities, L (length), M (mass), and T (time). Conversion for secondary entities such as pressure or velocity are deduced from the previous factors. Three independent primary conversion factors are needed, chosen to be, in our case, length, dynamic viscosity and density. Figure 11 is extracted from our MATLAB© code; the 2D image has a resolution of (NX*NY) pixels and the pixel size is known. "Phys" refers to physical units, and "Lat" to Lattice units. The pre-process to LBM algorithm (Physical to LBM units) and the post-process to LBM algorithm (LBM to Physical units) are shown. The LBM algorithm itself is omitted.

5.3.2. Advanced conversion: 2D to 3D resistivity

As shown in Fig. 11, the last instruction concerns deriving a 3D resistivity from the 2D computation. Indeed, the 2D situation does not correspond to the real 3D situation of Fig. 4. It corresponds to a 3D situation where the 2D pattern repeats itself in the third direction; velocities are compelled to stay in-plane.

Therefore, an ad hoc corrective formula is used where it is considered that a fluid particle can escape in the direction 3 constrained by a pattern identical to the one of the direction 2. For a square cylinder, the following relation can be written $\langle |v_t| \rangle = \sqrt{\langle |v_2| \rangle^2 + \langle |v_3| \rangle^2}$, with v_t being the velocity of the particle in the (2,3) planes, and v_2 and v_3 being its components in the respective directions 2 and 3. $\langle |v_3| \rangle = \langle |v_2| \rangle$ by hypothesis, leading to

```
% From physical to LBM units
Phys_H = NY*PixelSize %(m)
Phys_Dyn_Visco = 1.84e-5 %(Pa/s)
Phys_Density = 1.225 %(kg/m3)
Phys_Gravity = 9.81 %(m/s2)
Phys_Kin_Visco = Phys_Dyn_Visco/Phys_Density %(m2/s)
%
Lat_H = NY
Lat_Density=1.0
Lat_Tau =0.66 % chosen by the user
%
%Conversion: Phys_Q = Lat_Q x Coef_Q
Coef_H = Phys_H/Lat_H
Coef_Density = Phys_Density/(Lat_Density)
Lat_Kin_Visco = (Lat_Tau - 0.5)/3.0
Coef_t = Lat_Kin_Visco* Coef_H *Coef_H / Phys_Kin_Visco

% Coef deduced
Coef_u = Coef_H/Coef_t
Coef_F = Coef_Density*Coef_H^4/Coef_t^2
%
Phys_dPdL = 20.0 % (Pa/m) chosen by the user
Lat_dPdL = Phys_dPdL/Coef_Density/Coef_H*Coef_t*Coef_t

----- LBM algorithm

%From LBM to physical
Phys2_K0 = Coef_H*Coef_H*Lat2_K0_Darcy_Porous %(m2)
Phys2_Res = Phys_Dyn_Visco / Phys2_K0 %(Pa.s/m2)
Phys3D_Res = Phys2_Res / correctiveFactor
```

Figure 11: Pre and post process for units conversion.

$\langle |v_t| \rangle = \sqrt{2} \langle |v_2| \rangle$, with $\langle |v_2| \rangle = \phi \frac{\int_A |v_2| da}{\int_A da}$ being the mean of the module of the velocity in that direction. As the permeability can be sighted as an effective area, which resumes to a line for 2D calculations, it is suggested to modify this effective length line from a factor of $\sqrt{2}$. Therefore, in the following study, the 3D resistivity is deduced from the 2D calculations with the following formula: $\sigma_{3D} = \frac{\sigma_{2D}}{\sqrt{2}}$.

Establishing a general empirical or mathematical formula would be an interesting topic of investigation, however out of the scope of the present study. We would like to point out that any general formula could be simply analyzed numerically, comparing 3D and 2D calculations and generating random samples in order to cover the range of interest of the technical parameters of the acoustic materials. Concerning the porosity, which is recalled and indicated in the coming slice by slice analysis (see Table 3 and Table 4), it can be noticed that once the volume is discretized into voxels, the porosity can be evaluated slice by slice. In order words, at the difference of the resistivity, the porosity is independent on the size of the problem.

580 *5.4. Numerical convergence*

The size of the model (the lattice) is imposed, in our case, by the resolution of the image, given in pixels, and by the pixels dimension. From this, the remaining parameters to be set by the user are the relaxation time and the value of the pressure gradient. Calculation is followed looking at the evolution of the software tolerance $|V_1(iter) - V_1(iter - 1)|$, where V_1 is the mean value of the macroscopic velocity of the fluid phase in the direction 1, and following up the convergence of our main indicator, the 3D resistivity. Images of the airflow are from time to time examined.

585 *5.4.1. Relaxation parameter*

Convergence is typically of three types: i) an overshoot of the converged value and next decreasing oscillations towards the converged value, ii) a convergence from upper or lower values with or without weak oscillations, iii) spurious behavior with a phase with no convergence followed neither convergence nor divergence. The latter behavior was not observed. When divergence occurred, it happened within the first 1,000 iterations over the 20,000 iterations generally considered. Figure 12 presents typical convergence curves obtained when changing the values of the relaxation time.

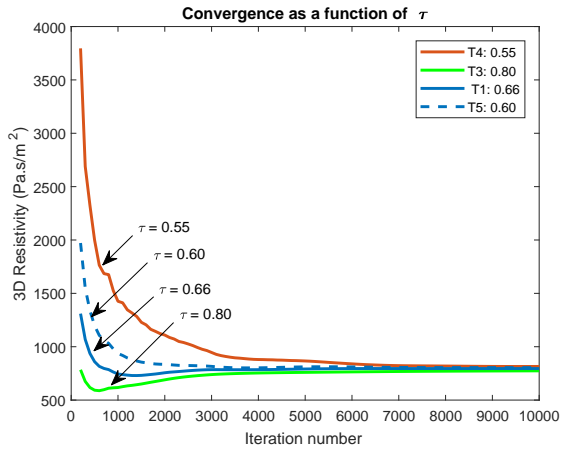


Figure 12: Convergence curves for different relaxation time values.

590 *5.4.2. Pressure gradient*

Pressure gradient is input in physical units. When water gravity problems are considered (as Darcy did with a column of water going through

610 sand), the pressure gradient is therefore $\vec{\nabla}p = \rho\vec{g}$ and leads to an intensity of $1000 \times 9.81 \approx 10000(N/m^3)$. If an air column is considered the intensity of the body force is $1.225 \times 9.81 \approx 10(N/m^3)$. The calculations are explored in this range and next extended to lower values. The very question is to stay in the domain of validity of LBM-BKG, which also fulfills the resistivity definition. In order words, the static airflow resistivity has to remain constant for quasi-static calculations. Fig. 13 shows the results obtained on a given sample, all calculations are conducted with $\tau = 0.66$ and up to 20,000 iterations, except for the last point, $\vec{\nabla}p = 1000$, where it was necessary to tune τ to 0.55 to have convergence. For further analyses, the couple of inputs $(\tau, \vec{\nabla}p)$ are chosen to be (0.66, 20) to satisfy the hypothesis and to produce convergence within 20,000 iterations.

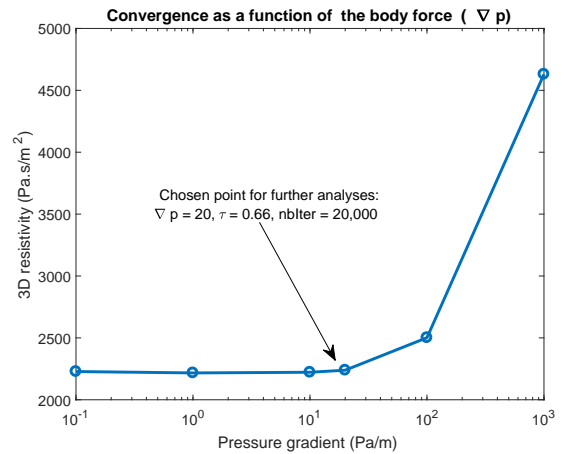


Figure 13: Adjusting of $\vec{\nabla}p$ to fit the LBM hypotheses and the resistivity definition.

630 *5.4.3. Tensorial simulated verification*

A sample is put in our numerical tube and the resistivity calculated. Next, the sample is turned 90° , once again 90° , and once again by 90° . The directions are called respectively, 1,2,3, and 4. Table 2 shows the results obtained. They conform to the theory stating that if the pressure gradient is inverted, the airflow reverts its direction resulting in an exactly inverted velocity field.

635 *5.4.4. Velocity fields*

As mentioned before, the visualization of the velocity field is also followed up from time to time.

Table 2: Porosity in opposite directions, Dir3 = -Dir1 and Dir4 = -Dir2.

	Resistivity		Resistivity
Dir1	1.5225e+03	Dir2	1.6726e+03
Dir3	1.5226e+03	Dir4	1.6724e+03

640 What is observed is that iteration by iteration the streamlines re-enforce up to convergence. Fig. 14 shows these streamlines (in blue).

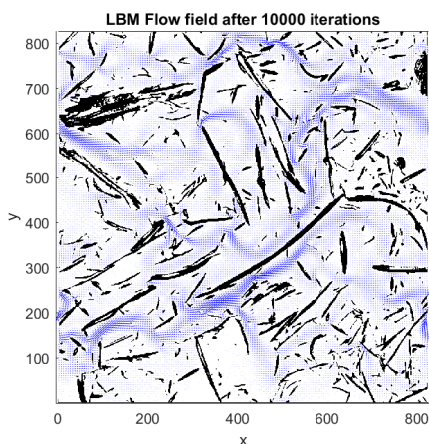


Figure 14: Flow field streamlines through a porous sample.

5.5. Resistivity estimation results

645 According to previous sections, a set of 10 slices is analyzed, extracted from the same set of slices used to estimate the porosity. The first slice, numbered 150, is selected; next, the slices 200, 300, ..., 900 and 939 (the last one) are selected. For each slice, the resistivity is calculated in both directions 1 and 2.

650 The results are reported in Table 3, where the lowest and highest value are, respectively, $853.4 Pa.s/m^2$ and $2242.8 Pa.s/m^2$. The label *Res* refers to the resistivity of a slice as the mean value of the resistivity tensor: $Res = (Res1 + Res2)/2$. The highest difference between slices is obtained considering the slice 150 ($2165 Pa.s/m^2$) and the slice 800 ($1091 Pa.s/m^2$). This difference is of $1074 Pa.s/m^2$. The slice giving the largest difference from one direction to another is the slice 700, with a difference of $656 Pa.s/m^2$. As it will be explained in the following paragraph, these differences are not significant in terms of engineering acoustics; however, as

665 we are in the case of very low resistivity, such differences may turn the value of resistivity from one slice to another of a single slice to double. The fundamental reason for that, to our view, is that a single slice is not representative of the actual representative volume. If the representative volume were the smallest possible representative volume, all the 790 slices available should be considered. That is why it is interesting to notice that the statistic mean value obtained of $1382 \pm 12 (Pa.s/m^2)$, using this set of 10 slices, already gives a close approximation to the measured reference value of $1350 Pa.s/m^2$, obtained using a resistivity-meter. The reference values are labeled as RefTest in Table 3.

670 Ten samples is a low number in terms of usual statistics. Therefore, aiming to confirm the results obtained, the analysis is extended by considering two larger set of slices: the first one with 17 slices, namely 150, 200, 250, ..., and the second one with 33 slices, namely 150,175, 200, 225, ..., 939. Extremal values of $3487 Pa.s/m^2$ (slice 275) and of $776 Pa.s/m^2$ (slice 750) are encountered without significantly modifying the mean values reported in Table 4. The standard error also converges, which reinforces the results. The porosity is also analyzed, and no relation is found between the variation in porosity, from one slice to another, and the corresponding variation in resistivity.

Table 3: LBM analysis of a sample of 10 slices, labeled according to the tomographic imaging order, and their respective porosities, resistivities *Res1* and *Res2* in directions 1 and 2, mean values of each resistivity tensor $Res = (Res1 + Res2)/2$, the resulting Mean porosity and *Res*, and the measured values RefTest. Resistivities in $Pa.s/m^2$.

Slice	Porosity	<i>Res1</i>	<i>Res2</i>	<i>Res</i>
150	0.842	2242.8	2086.4	2165
200	0.857	1264.1	1360.6	1312
300	0.844	1690.2	1490.1	1590
400	0.873	1229.0	942.9	1086
500	0.868	1066.4	1335.2	1201
600	0.862	1081.8	1318.7	1200
700	0.861	2089.0	1432.5	1761
800	0.865	1126.6	1056.0	1091
900	0.864	853.4	1380.0	1117
939	0.867	1193.0	1402.8	1298
Mean	0.860 ± 0.009	1382 ± 12		
RefTest	0.866	1350		

Table 4: LBM analysis of sets of 10, 17 and 33 slices with the respective mean porosities and mean Res , and the measured values RefTest. Resistivities in $Pa.s/m^2$.

Number of Slices	Mean Porosity	Mean Res
10	0.860 ± 0.009	1382 ± 12
17	0.863 ± 0.003	1336 ± 09
33	0.863 ± 0.003	1370 ± 07
RefTest	0.866	1350

5.6. Discussion

To deepen into the analysis of the results, several considerations are made in the following, which are important to illustrate and contextualize this investigation.

5.6.1. Sensitivity to global acoustic indicators

The airflow resistivity is a parameter that covers a large range of values, generally from 10,000 to 100,000 $Pa.s/m^2$, for common acoustic materials. Thus, with an estimate mean resistivity of 1,382 $Pa.s/m^2$, calculated from actual values ranging from 853.4 to 2,242.8 $Pa.s/m^2$ (see Table 3), our sample sits in the range of very low resistivities. It is shown in this part that, sighted from the two usual main global acoustic indicators - absorption and transmission loss (TL) - the seemingly large range of values should be considered actually close.

For example, a resistivity of 1,000 $Pa.s/m^2$ would produce quasi-identical absorption and TL curves compared to the ones produced by a resistivity of 2,000 $Pa.s/m^2$, while a resistivity of 20,000 $Pa.s/m^2$ would produce very different results than a resistivity of 40,000 $Pa.s/m^2$, although the proportion involved is the same for both cases.

The formulae of the JCA fluid equivalent model described in paragraph 3.2 are implemented in the semi-analytical Matlab transfer matrix code named TMTX. Fig. 15 and Fig. 16 show, respectively, the absorption and the TL curves obtained using TMTX when various resistivities are considered. The other parameters of the simulation are: $\phi = 0.86$, $\alpha_\infty = 1$, $\Lambda = 167.3\mu m$ and $\Lambda' = 334.6\mu m$. The thickness of the sample is 40mm, and normal incident acoustic waves are considered. For the range of variation of our parameter (Min, Nominal, Max), the curves are, indeed, superimposed.

5.6.2. Representative volume

The results presented in Table 3 indicate that, for a given slice, the resistivity calculated in direction

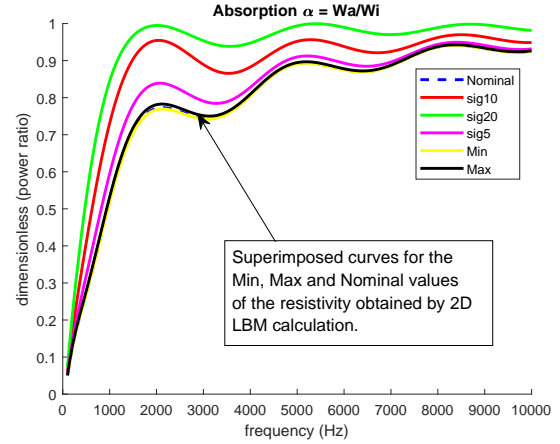


Figure 15: Absorption curves for $\sigma = 10,000$ (sig10), $\sigma = 20,000$ (sig20), $\sigma = 5,000$ (sig5), $\sigma = 853.4$ (Min), $\sigma = 2,242.8$ (Max) and $\sigma = 1,382$ (Nominal).

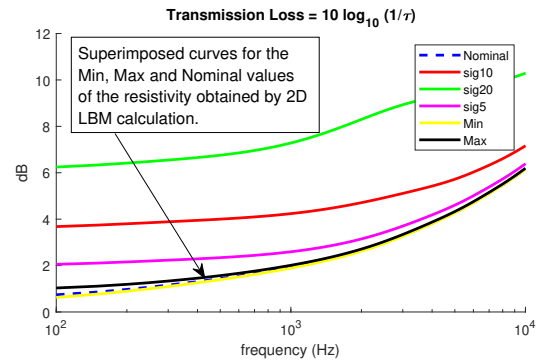


Figure 16: Transmission Loss curves for $\sigma = 10,000$ (sig10), $\sigma = 20,000$ (sig20), $\sigma = 5,000$ (sig5), $\sigma = 853.4$ (Min), $\sigma = 2,242.8$ (Max) and $\sigma = 1,382$ (Nominal).

1 is close to the one calculated in direction 2, while the difference in resistivity from one slice to another is larger. From our point of view, this is due to two combined facts: i) the fact, already mentioned in paragraph 5.1, that the manufactured process tends to layer the material, and ii) the fact that the tomography images are also acquired in the plane of this slightly layered material. Finally, our material is slightly orthotropic. The slice producing the larger resistivity is the slice 150, which is the slice shown in Fig. 6. The slice producing the lowest resistivity is the slice 900, which is the image used in Fig. 14. It can be seen that the slice producing the larger resistivity is the slice with more fiber obstacles.

At this stage, the important point to underline is that a single image is not representative of the volume sample of the material. The volume sample, itself, is considered to be a representative volume of the material. That is why it is needed to consider several slices. For each slice, the mean value of the resistivity tensor component in directions 1 and 2 is considered. This is a meaningful value sighted from tensor theory, where the mean value is invariant (per rotation). Next, the mean value of the mean value of each slice is considered. The results obtained are satisfactory from a statistical point of view, turning out to be close to the reference measured values and with low data dispersion (standard deviation).

6. Conclusions

We have explored the possibility of estimating both porosity and airflow resistivity of an acoustic fibrous material from X-ray Computed Tomography 2D images. This porous material, constituted of coconut fibers, was selected due to its sustainability interest, low cost, and challenging characterization. Initially, a 3D image of each of various samples was generated by piling up a large set of transversal slices. Then, we deduced the resulting mean porosity making use of several methods, the performances of which were properly compared. Next, we applied the Lattice Boltzmann Method (LBM) to estimate the static airflow resistivity. Mean values were obtained from the analysis of ten slices per sample. We have shown that, for the first time according to our knowledge, a simple 2D implementation of LBM of low computational cost was successful in characterizing this fibrous material, which is intrinsically difficult due to its highly anisotropic micro-structure. The results are very consistent with tests carried out using a porosity-meter and an airflow resistivity-meter. The numerical approach led to a porosity of 0.86 and a resistivity of $1382 Pa.s/m^2$, while the directly measured values were 0.87 and $1350 Pa.s/m^2$, respectively. We believe these results suggest the potential use of this implementation to characterize other fibrous materials.

Acknowledgments

The authors would like to thank the CAPES-COFECUB Project 773/13 - Proc. 8909-14-8, the CNPq/Universal Proc. 82351/2013-6 and the

CAPES/PNPD Proc. 1564115 for their financial support. We would also like to thank Jean-Daniel Chazot, from the Laboratoire Roberval (UMR CNRS 7337) of the Université de Technologie de Compiègne (UTC)/France, and Benjamin Smaniotto, Technical Manager of the tomograph of the Laboratoire de Mécanique et Technologie (LMT, UMR CNRS 8535) of the ENS Paris-Saclay, for their valuable help.

Appendix A. LBM-BGK method

The Lattice Boltzmann Method (LBM) can be seen as a spacial and temporal finite difference method which takes benefit of a mesh (the lattice) that has to be strictly constructed with square elements with $\Delta x = \Delta y = \Delta t$ for each element. Doing this, it is possible to solve the Boltzmann transport equation

$$\frac{\partial f}{\partial t} + \vec{v} \cdot \vec{\nabla} f = \Omega. \quad (\text{A.1})$$

This equation is an equilibrium equation where $f(\vec{x}, t)$ is the particle distribution function, $\vec{v}(\vec{x}, t)$ is the particle velocity, and Ω is the collision operator. The equilibrium is found iteratively. The main references used in this section are [40, 41, 42].

Appendix A.1. Streaming and equilibrium

Using the D2Q9 model, shown in Fig. A.17, the particle is restricted to stream in 9 possible directions described by the microscopic velocities \vec{e}_i , where the index $i \in \{0, 1, 2, \dots, 8\}$, with $i = 0$ being attributed to the particle at rest. For each direction is also associated a probability function f_i . As important remarks: the vectors \vec{e}_i do not change during the process, in opposition to their associated distribution functions; the vectors \vec{e}_i on the diagonals are of $\sqrt{2}$ length, while the others are unitary.

The macroscopic fluid density $\rho(\vec{x}, t)$ and the macroscopic velocity $\vec{v}(\vec{x}, t)$ at each Lattice node can be extracted from the probability distribution functions of the particle by the equations

$$\rho = \sum_i f_i, \quad \rho \vec{v} = \sum_i f_i \vec{e}_i, \quad (\text{A.2})$$

and the pressure p can be evaluated from the density as $p = \rho c_s^2$, where $c_s = 1/\sqrt{3}$ is the lattice speed of sound.

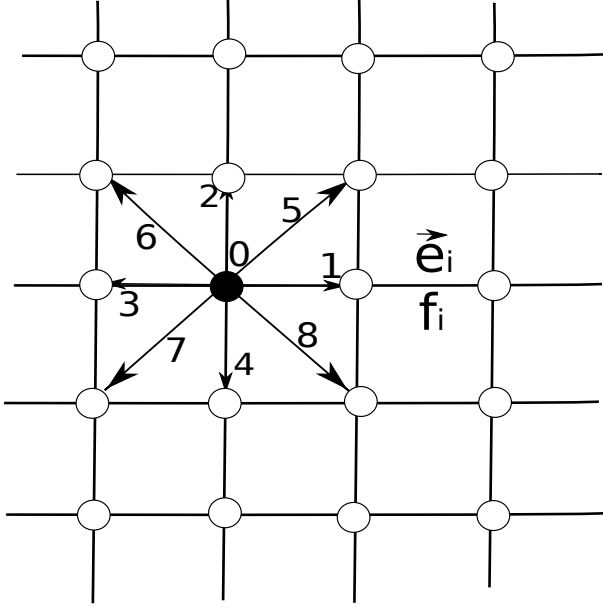


Figure A.17: D2Q9 discretization scheme.

Using the D2Q9 discretization and the Bhatnagar-Gross-Krook (BGK) collision model (that suffices for laminar single phase flows), Eq. A.1 can be rewritten as

$$f_i(\vec{x} + c\vec{e}_i\Delta t, t + \Delta t) - f_i(\vec{x}, t) = -\frac{f_i(\vec{x}, t) - f_i^{eq}(\vec{x}, t)}{\tau}, \quad (\text{A.3})$$

with τ being a relaxation time, and f_i^{eq} the equilibrium distribution. Reorganizing Eq. A.3 allows for the calculation of the distribution at $t + \Delta t$ from the distribution at t as

$$f_i(\vec{x} + c\vec{e}_i\Delta t, t + \Delta t) = f_i(\vec{x}, t) - \frac{f_i(\vec{x}, t) - f_i^{eq}(\vec{x}, t)}{\tau}. \quad (\text{A.4})$$

f_i^{eq} is evaluated from the macroscopic density and velocity as

$$f_i^{eq}(\vec{x}, t) = \omega_i \rho \left(1 + 3 \frac{\vec{e}_i \cdot \vec{v}}{c^2} + \frac{9}{2} \frac{(\vec{e}_i \cdot \vec{v})^2}{c^4} - \frac{3}{2} \frac{\vec{v} \cdot \vec{v}}{c^2} \right), \quad (\text{A.5})$$

where ω_i are weight factors: $\omega_i = 4/9$ for $i = 0$, $\omega_i = 1/9$ for $i = 1, 2, 3, 4$ and $\omega_i = 1/36$ for $i = 5, 6, 7, 8$. In the previous equation $c = \Delta x / \Delta t$ is the lattice speed, which is taken to be 1.

Another relation links the fluid kinematic viscosity μ to the relaxation time τ by

$$\mu = \frac{2\tau - 1}{6} \frac{(\Delta x)^2}{\Delta t}. \quad (\text{A.6})$$

The first term of the second member of Eq. A.4 refers to the streaming phase, while the second one to the collision phase. These two phases are generally separated in the programming process.

Appendix A.2. Boundary conditions

Imposing boundary conditions within the LBM is not a straightforward process because the macroscopic Navier-Stokes boundary conditions must be translated to microscopic boundary conditions on f_i and f_i^{eq} . Boundary conditions are generally of the following types:

- Bounce Back: No-Slip Boundary Conditions;
- Boundary Conditions with Known Velocity;
- Periodic Boundary Conditions;
- Imposed Pressure Difference Boundary Conditions.

Our code is strictly limited to the resolution of our given problem. It is described, hereafter, the two types of boundary conditions considered: i) a Bounce Back scheme and ii) imposed body forces (which is a non standard type) of constant value and orientation.

i) Bounce back. It concerns the reflection of the particles on the fixed obstacles (the fibers of the porous samples). A full-way model of bounce-back is preferred to a mid-way one since the first does not require to know the normal orientation when a particle enters in contact with a rigid boundary. This model is adapted when several obstacles are present. At a first step, the fixed lattice nodes in contact with the wet area are to be considered in the streaming process. Next, the particle distribution functions of these nodes, which point to the exterior of the fluid area, are reversed in direction.

ii) Body forces. We intend, from the definition of the permeability (Eq. 7), to impose a pressure gradient (a body force) all over the fluid domain. This leads to the advanced developments studied in [42] because the body forces have to be added to the initial equilibrium Eq. A.3:

$$f_i(\vec{x} + c\vec{e}_i\Delta t, t + \Delta t) - f_i(\vec{x}, t) = -\frac{f_i(\vec{x}, t) - f_i^{eq}(\vec{x}, t)}{\tau} + \Delta t F_i, \quad (\text{A.7})$$

where F_i are the body forces.

Theoretically, all previous formulae A.1 to A.5 should be modified. However, [42] shows that when the body forces are slightly changing in space and time, the representation of the body as $F_i = \omega_i \vec{e}_i \cdot \vec{F} / c_s^2$ can be directly introduced in the previous model unaltered, and the Navier-Stokes equations remain verified.

Appendix A.3. Algorithm

Finally, using the notation $:=$ as the programming affectation operator, our algorithm for a current iteration is the following:

- $f_i(\text{iter} + 1) := Pr(f_i(\text{iter}))$ (propagation);
- $f_i(\text{iter} + 1) := f_i(\text{iter} + 1) + F_i$, (body forces);
- $f_i(\text{iter} + 1) := Bb(f_i(\text{iter} + 1))$ (bounce-back);
- $\rho := \sum_i f_i(\text{iter} + 1)$; $\vec{v} := \sum_i f_i(\text{iter} + 1)\vec{e}_i / \rho$ (macro);
- $f_i^{eq}(\rho, \vec{v})$ (equilibrium);
- $f_i(\text{iter} + 1) := f_i(\text{iter} + 1) - \frac{f_i(\text{iter} + 1) - f_i^{eq}}{\tau}$ (collision).

References

References

- [1] M. A. Biot, Theory of propagation of elastic waves in a fluid-saturated porous solid. I. Low-frequency range. II. Higher frequency range, *JASA* 28 (1956) 168–191. doi:10.1121/1.1908239, 10.1121/1.1908241.
- [2] J. F. Allard, N. Atalla, *Propagation of Sound in Porous Media: Modeling Sound Absorbing Materials*, 2nd Edition, Wiley, 2009.
- [3] K. V. Horoshenkov, A review of acoustical methods for porous material characterization, *International Journal of Acoustics and Vibration* 22 (2017) 92–103. doi:10.20855/ijav.2017.22.1455.
- [4] Z. L. Liu, *Multiphysics in Porous Materials*, Springer, 2018. doi:10.1007/978-3-319-93028-2.
- [5] O. Doutres, Y. Salissou, N. Atalla, R. Panneton, Evaluation of the acoustic and non-acoustic properties of sound absorbing materials using a three-microphone impedance tube, *Applied Acoustics* 71 (2010) 506–509. doi:10.1016/j.apacoust.2010.01.007.

- [6] F. C. Bannwart, L. F. Cóser, B. N. Huallpa, D. A. Siviero, J. F. R. Arruda, On the effects of air cavity backing porous materials for its characterization by the three-microphone method, in: *Proc. of the 34th Int. Conf. on Noise and Vibration Engineering (ISMA2016)*, Leuven, Belgium, September 19–21, 2016, pp. 33–46. doi:10.13140/RG.2.2.24667.36642.
- [7] A. Abbad, N. Atalla, M. Ouisse, O. Doutres, Numerical and experimental investigations on the acoustic performances of membraned helmholtz resonators embedded in a porous matrix, *Journal of Sound and Vibration* 459 (2019) 1–17. doi:10.1016/j.jsv.2019.114873.
- [8] Y. Atalla, R. Panneton, Low frequency inverse method for the identification of the viscous and thermal characteristic lengths of porous media, in: *Int. Congress on Noise Control Engineering*, Fort Lauderdale, Florida, U.S.A., December 06–08, 1999.
- [9] O. Doutres, Y. Salissou, N. Atalla, R. Panneton, Inverse acoustical characterization of open cell porous media using impedance tube measurements, in: *Can. Acoust.*, Vol. 33, 2005, pp. 11–24.
- [10] M. Guédra, F. C. Bannwart, G. Penelet, P. Lotton, Parameter estimation for the characterization of thermoacoustic stacks and regenerators, *Applied Thermal Engineering* 80 (2015) 229–237. doi:10.1016/j.applthermaleng.2015.01.058.
- [11] T. Zielinski, Normalized inverse characterization of sound absorbing rigid porous media, *JASA* 137 (2015) 3232–3243. doi:10.1121/1.4919806.
- [12] Y. Yang, Z. Chen, A model for calculating the air flow resistivity of glass fiber felt, *Applied Acoustics* 91 (2015) 6–11. doi:10.1016/j.apacoust.2014.11.006.
- [13] A. I. Hurrell, K. V. Horoshenkov, M. T. Pelegrinis, The accuracy of some models for the airflow resistivity of nonwoven materials, *Applied Acoustics* 130 (2018) 230–237. doi:10.1016/j.apacoust.2017.09.024.
- [14] P. Soltani, E. Taban, M. Faridan, S. E. Samaei, S. Amininasab, Experimental and computational investigation of sound absorption performance of sustainable porous material: *Yucca gloriosa* fiber, *Applied Acoustics* 157 (2019) 1–12. doi:10.1016/j.apacoust.2019.106999.
- [15] G. Ji, J. Cui, Y. Fang, S. Yan, J. Zhou, J.-K. Kim, Nano-fibrous composite sound absorbers inspired by owl feather surfaces, *Applied Acoustics* 156 (2019) 151–157. doi:10.1016/j.apacoust.2019.06.021.
- [16] L. C. G. Pennafort, *Aplicação da mecânica da danificação na análise do comportamento de materiais compósitos poliméricos reciclados reforçados por fibras de coco*, Ph.D. thesis, Universidade Federal de Ceará (2014).
- [17] H. Taud, R. Martinez-Angeles, J. F. Parrot, L. Hernandez-Escobedo, Porosity estimation method by x-ray computed tomography, *J. Petroleum Sci. and Eng.* 47 (2005) 209–217. doi:10.1016/j.petrol.2005.03.009.
- [18] P. G. K. Gao, J. A. W. van Dommelen, M. G. D. Geers, Computational homogenization of sound propagation in a deformable porous material including microscopic viscous-thermal effects, *Journal of Sound and Vibration* 365 (2016) 119–133. doi:10.1016/j.jsv.2015.11.037.
- [19] T. Zielinski, Microstructure representations for sound absorbing fibrous media: 3d and 2d multiscale modelling and experiments, *Journal of Sound and Vibration* 409 (2016) 112–130. doi:10.1016/j.jsv.2017.07.047.

- [20] J. Y. Chung, D. A. Blaser, Transfer function method of measuring in-duct acoustic properties. ii. experiment, *JASA* 68 (1980) 914–921. doi:10.1121/1.384779.
- [21] O. Tanneau, J.-B. Casimir, P. Lamary, Optimization of multilayered panels with poroelastic components for an acoustical transmission objective, *JASA* 120 (2006) 1227–. doi:10.1121/1.2228663.
- [22] B. Brouard, B. Castagnède, M. Henry, D. Lafarge, S. Sahraoui”, Mesure des propriétés acoustiques des matériaux poreux, Techniques de l’ingénieur Acoustique : mesures, contrôle, applications base documentaire : TIB423DUO. (ref. article : r6120), fre. arXiv: basedocumentaire:TIB423DUO.
- [23] N. A. O. Doutres, H. Osman, Transfer matrix modeling and experimental validation of cellular porous material with resonant inclusions, *JASA* 137 (2015) 3502–3513. doi:10.1121/1.4921027.
- [24] O. Tanneau, P. Lamary, Y. Chevalier, A boundary element method for porous media, *JASA* 120 (2006) 1239–. doi:10.1121/1.2228663.
- [25] P. Lamary, R. de Araújo Bezerra, I. da Silva Júnior, E. D. de Pontes, A. Benallal, A multi-physic implementation of the finite element method applied to research on acoustic poro-elastic materials, in: CIL-AMCE 2014, Fortaleza, 2014, 10.13140/2.1.2515.2327. doi:10.13140/2.1.3301.6644.
- [26] R. Rumpler, Efficient finite element approach for structural-acoustic applications including 3d modelling of sound absorbing porous materials, Ph.D. thesis, KTH, MWL Numerical acoustics, qC 20120224 (2012).
- [27] N. Dauchez, P.-A. Yvars, Inverse method for porous material characterization using the constraint satisfaction problem approach, in: Acoustics 2012, Nantes, 2012.
- [28] AFPC-AFREM, Détermination de la masse volumique apparente et de la porosité accessible à l’eau - méthodes recommandées pour la mesure des grandeurs associées à la durabilité, in: Compte-rendu des Journées Techniques, Toulouse, 11-12 Décembre 1997, 1997, pp. 121–124.
- [29] Y. Salissou, R. Panneton, Pressure/mass method to measure open porosity of porous solids, *J. Appl. Phys.* 101, 2007, 124913: 1-7. doi:10.1063/1.2749486.
- [30] A. Keller, High resolution, non-destructive measurement and characterization of fracture apertures, *Int. Journal Rock Mech. Min. Sci.* 35(8) (1998) 1037–1050. doi:10.1016/S0148-9062(98)00164-8.
- [31] T. W. Ridler, S. Calvard, Picture thresholding using an iterative selection method, *IEEE Transactions on Systems, Man and Cybernetics* 8 (1978) 630–632. doi:10.1109/TSMC.1978.4310039.
- [32] L. K. Huang, M. J. J. Wang, Image thresholding by minimizing the measures of fuzziness, *Pattern Recognition* vol 23 No. 1 (1995) 41 – 51. doi:10.1016/0031-3203(94)E0043-K.
- [33] C. H. Li, C. K. Lee, Minimum cross entropy thresholding, *Pattern Recognition* 26, No 4 (1993) 617–625. doi:10.1016/0031-3203(93)90115-D.
- [34] C. A. Glasbey, An analysis of histogram-based thresholding algorithms, *CVGIP: Graphical Models and Image Processing* 55 (1993) 532–537. doi:10.1006/cgip.1993.1040.
- [35] W. H. Tsai, Moment-preserving thresholding: a new approach, *Computer Vision, Graphics, and Image Processing* 29 (1985) 377–393. doi:10.1016/0734-189X(85)90133-1.
- [36] N. Otsu, A threshold selection method from gray-level histograms, *IEEE Transactions on systems, Man, and Cybernetics SMC-9*, No. 1, January (1979) 62 – 66. doi:10.1109/TSMC.1979.4310076.
- [37] A. G. Shanbhag, Utilization of information measure as a means of image thresholding, *CVGIP: Graphical Models and Image Processing* vol 56 No 5 (1994, September) 414–419. doi:10.1006/cgip.1994.1037.
- [38] C. V. der Kelen, P. Göransson, Identification of the full anisotropic flow resistivity tensor for multiple glass wool and melamine foam samples, *JASA* 134 (2013) 46–59. doi:10.1121/1.4824841.
- [39] T. Krüger, Unit conversion in lbm, in: LBM Workshop, Edmonton, Canada, 2011.
- [40] Y. Bao, J. Meskas, Lattice boltzmann method for fluid simulations, Tech. rep., New York University, Department of Mathematics (2011).
- [41] P. Wang, Lattice boltzmann simulation of permeability and tortuosity for flow through dense porous media, *Mathematical Problems in Engineering* Article ID 694350 (2014). doi:10.1155/2014/694350.
- [42] Z. Guo, C. Zheng, B. Shi, Discrete lattice effects on the forcing term in the lattice boltzmann method, *PHYSICAL REVIEW E* 65, 046308 (2002). doi:10.1103/PhysRevE.65.046308.